Article

Estimation of Ground-Level PM$_{2.5}$ Concentration at Night in Beijing-Tianjin-Hebei Region with NPP/VIIRS Day/Night Band

Yu Ma [1,2] 🔵, **Wenhao Zhang** [1,2,*] 🔵, **Lili Zhang** [3], **Xingfa Gu** [3] **and Tao Yu** [3]

1 School of Remote Sensing and Information Engineering, North China Institute of Aerospace Engineering, Langfang 065000, China
2 Hebei Collaborative Innovation Center for Aerospace Remote Sensing Information Processing and Application, Langfang 065000, China
3 Aerospace Information Research Institute, Chinese Academy of Sciences, Beijing 100094, China
* Correspondence: zhangwh@radi.ac.cn

Abstract: Reliable measures of nighttime atmospheric fine particulate matter (PM$_{2.5}$) concentrations are essential for monitoring their continuous diurnal variation. Here, we proposed a night PM$_{2.5}$ concentration estimation (NightPMES) model based on the random forest model. This model integrates the radiance of the Visible Infrared Imaging Radiometer Suite (VIIRS) Day/Night Band (DNB), moon phase angle, and meteorological data. We collected 13486 samples from the Beijing Tianjin–Hebei (BTH) region. The determination coefficient (R^2) of the NightPMES model was 0.82, the root mean square error (RMSE) was 16.67 μg/m^3, and the mean absolute error (MAE) was 10.20 μg/m^3. The applicability analysis of the moon phase angles indicated that the amount of data available increased by 60% while the accuracy remained relatively unchanged. In the seasonal model, the meteorological factors and DNB radiance were found to be the primary factors affecting the PM$_{2.5}$ concentration in different seasons. In conclusion, this study provided a method for estimating nighttime PM$_{2.5}$ concentration that will improve our understanding of air pollution and associated trends in PM$_{2.5}$ variation.

Keywords: VIIRS/DNB; nighttime PM$_{2.5}$; moon phase angle; BTH; random forest

1. Introduction

PM$_{2.5}$ is a fine particulate matter (PM), which has an aerodynamic hollow diameter $\leq$2.5 μm, and is one of the main air pollutants [1]. To address increasing air pollution, the World Health Organization has recommended lowering the average annual PM$_{2.5}$ concentrations from 10 μg/m^3 to 5 μg/m^3 [2]. Long-term exposure to elevated PM$_{2.5}$ concentrations is established to cause health problems and increase mortality risk [3–8]. However, recent studies have found that even low PM$_{2.5}$ concentrations that meet the air-quality standards can increase the risk of premature death [9]. Thus, considerable attention has been devoted to investigating PM$_{2.5}$ sources, health effects, and long-term monitoring of its variation [10–12]. While satellite remote sensing has collected much data on daytime PM$_{2.5}$ concentrations, research at night is scarce. The lack of nighttime PM$_{2.5}$ data hampers research on its continuous temporal and spatial variation. Continuous monitoring of both day and nighttime PM$_{2.5}$ concentrations will help to better understand its formation and dissipation [13,14].

Strong correlations were found between PM$_{2.5}$ concentrations and aerosol optical depth (AOD). Hence, many AOD-PM$_{2.5}$ models have been constructed to estimate ground PM$_{2.5}$ concentrations [15–18]. For example, in order to create an ensemble model of the PM$_{2.5}$ concentration in the London region, Yazdi et al. [19] employed the AOD products from the Moderate Resolution Imaging Spectroradiometer (MODIS), land-cover type, and meteorological data as the inputs. The model comprised K-nearest neighbor, gradient-boosting machine, and random forest (RF). Using the Top-of-Atmospheric Reflectance

(TOAR) and meteorological data, Feng et al. [20] calculated the $PM_{2.5}$ concentrations in the BTH region. Directly using TOAR products avoids the intermediate process of AOD inversion and improves the accuracy. The characterization of TOAR at night requires accurate lunar irradiance at the top of the atmosphere. However, lunar irradiance varies dramatically depending on the variable of the moon phase and the geometry of the Sun/Earth/Moon [21]. At present, there is still a lack of high-precision lunar irradiance models and nighttime radiation transmission models to accurately describe the nighttime radiation transmission process. Therefore, it is difficult to obtain accurate TOAR and AOD at night, which limits their applications in estimating $PM_{2.5}$ concentrations.

The successful launch of the Suomi National Polar-Orbit Partnership (NPP) satellite has provided remote sensing data support for night monitoring of the atmosphere [22]. The first study of nighttime aerosols using a Visible Infrared Imaging Radiometer Suite (VIIRS) Day/Night Band (DNB) proposed obtaining nighttime aerosol optical depth from the difference between the observed urban light sources and dark background radiation [23]. Based on this study [23], McHardy et al. [24] proposed a spatial standard deviation (spatial derivative) for urban lighting to estimate nighttime atmospheric aerosols. This method does not require calculating the radiation of the dark background area without an artificial light source. Next, Zhang et al. [25] followed up on the methods of McHardy et al. using surface diffuse reflection to characterize the spatial variation in artificial light sources and then estimated nighttime AOD. More recently, a different study established a multiple linear regression (MLR) model with VIIRS/DNB, atmospheric water vapor content, air pressure, and $PM_{2.5}$ concentration in the Atlanta region based on the radiative transfer theory [26]. Thus, VIIRS/DNB-derived techniques demonstrate that nighttime $PM_{2.5}$ concentration can be measured. Subsequently, Zhao et al. [27] developed a nighttime $PM_{2.5}$ concentration inversion model based on the back propagation (BP) neural network using VIIRS/DNB radiance combined with meteorological variables (including relative humidity and temperature). The correlation coefficient of validation across 12 Beijing sites was 0.91, further verifying the feasibility of VIIRS/DNB radiance as a method to estimate nighttime $PM_{2.5}$ concentrations. Moreover, Fu et al. [28] established a mixed-effect model (MEM) between the VIIRS/DNB radiance and $PM_{2.5}$ concentration, and then tested it in both the light-intensive urban areas and light-sparse suburbs of Beijing. The correlation coefficients of the model were 0.95 ± 0.02 in the metropolitan area and 0.88 ± 0.06 in the suburbs. Furthermore, VIIRS/DNB radiance was found capable of estimating $PM_{2.5}$ concentrations in sparsely lit areas. Based on the relationship between $PM_{2.5}$ concentration and AOD, Erkin et al. [29] proposed a hybrid adaptive deep-learning algorithm. The input-independent variables were VIIRS/DNB_{AOD}, meteorological data, and auxiliary data, and the output was the $PM_{2.5}$ concentration. This study focused on the changes in the $PM_{2.5}$ concentration caused by fireworks in cities before, during, and after the Spring Festival. The results showed that the rapid increase in $PM_{2.5}$ concentration caused by the fireworks affected the monthly average concentration of $PM_{2.5}$ during the Spring Festival and that in the period after the Spring Festival.

Multiple linear regression, the mixed effect model, and various machine-learning methods have been involved in the study of nighttime $PM_{2.5}$ concentration estimation, but only data with a large moon phase angle are used to reduce the influence of moonlight. Therefore, this study selected VIIRS/DNB radiance under all moon phase angles and incorporated meteorological data to establish a multi-parameter comprehensive random forest model. Our aim was to validate this model for estimating the nighttime $PM_{2.5}$ concentration in the BTH region.

2. Materials and Methods

2.1. Data Collection

(1) Satellite data

The NPP is the first satellite of the National Polar-orbiting Operational Environmental Satellite System (NPOESS) from the United States. The VIIRS is one of the five major Earth

observing instruments onboard NPP. Its footprint field of view on the ground is 3060 km wide, and it obtains data from Earth twice a day with a repetition period of 16 days [30]. The VIIRS has 22 bands, including five high-resolution (I-band), 16 moderate-resolution (M-band), and one DNB [31].

In this study, three VIIRS datasets were used: (a) scientific data record (SDR) for M-band, including M12 and M15; (b) DNB geolocation SDR, including latitude, longitude, and moon phase angle; and (c) DNB radiances SDR. The DNB (0.5–0.9 μm) radiance data were conducted with geometric correction and radiometric calibration before use. These data have a spatial resolution of 750 m and are published daily in H5 format. Figure 1 shows the spectral response function of the band used [30]. Because the official website lacked cloud product data in 2021, this study used M12 (3.61–3.79 μm) and M15 (10.26–11.26 μm) of the VIIRS to identify and eliminate clouds. The M-band and DNB were obtained from https://www.avl.class.noaa.gov/, accessed on 15 March 2022 [32,33].
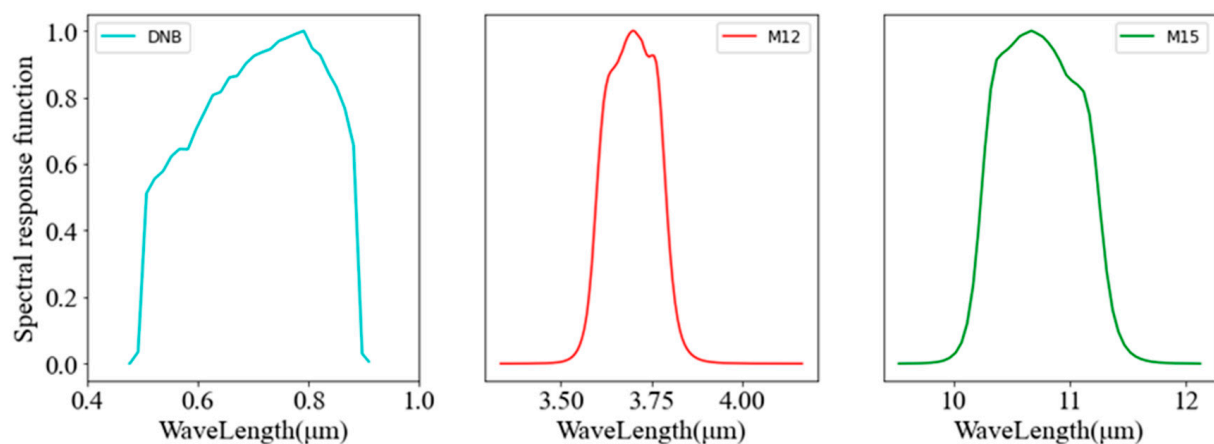

Figure 1. The DNB, M12, and M15 spectral response functions.

(2)   Meteorological data

The meteorological data for 2021 were obtained from the second Modern-Era Retrospective Analysis for Research and Applications (Merra-2) [34]. The planetary boundary layer height (PBLH), surface wind speed (WS), surface air temperature (AT), and surface pressure (SP) were the four variables included in the data. The surface relative humidity (RH) was calculated from the SP, AT, and surface-specific humidity (SH). The information is accessible at https://disc.gsfc.nasa.gov/datasets, accessed on 24 February 2022. All downloaded data were resampled to the same spatial resolution (0.007°) as that of the satellite data. The processed data were then used for model training and verification.

(3)   Ground $PM_{2.5}$ data

The ground $PM_{2.5}$ data of 2021 were collected from 121 state-controlled ground stations in the BTH region (Figure 2) and downloaded from the China Environmental Monitoring Center website: http://www.cnemc.cn/, accessed on 18 March 2022. Missing data were removed during processing [20]. Table 1 lists the specific datasets, including satellite, meteorological, and ground $PM_{2.5}$ data.
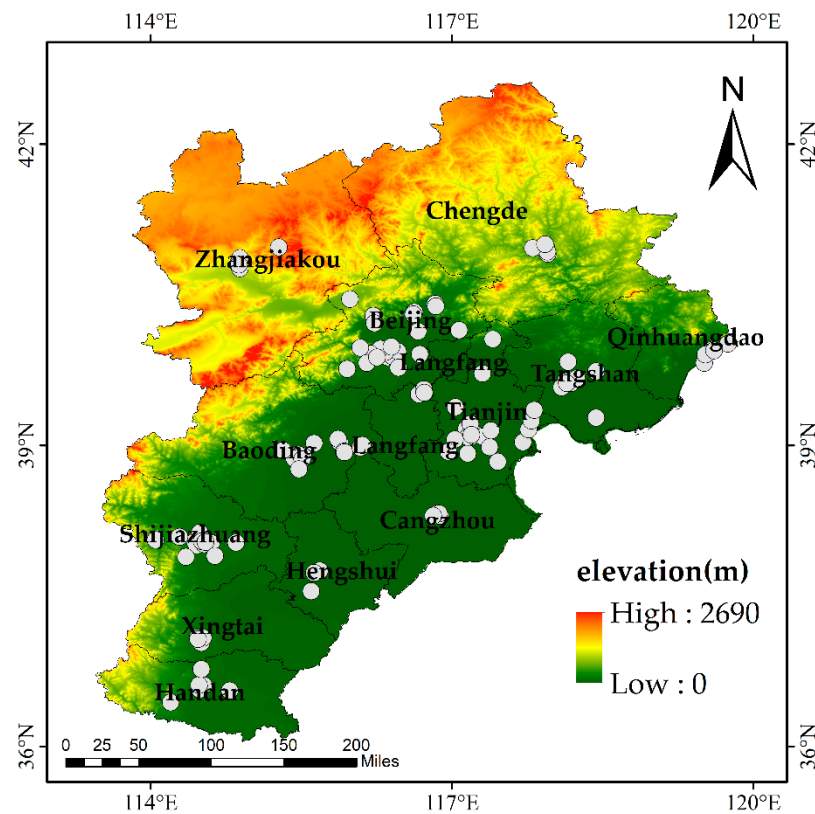
Figure 2. Elevation map of the BTH region. Ground PM$_{2.5}$ data were acquired from state-controlled ground stations (white dots).

Table 1. Dataset statistics.

Category	Variable	Units	Spatial Resolution	Temporal Resolution
Satellite data	DNB radiance	W/(sr·m^2)	750 m	Daily
	moon phase angle	degree	-	Daily
Meteorological data	PBLH [1]	m	0.5° × 0.625°	Hourly
	SP [2]	Pa	0.5° × 0.625°	Hourly
	AT [3]	K	0.5° × 0.625°	Hourly
	RH [4]	%	0.5° × 0.625°	Hourly
	WS [5]	m/s	0.5° × 0.625°	Hourly
Ground PM$_{2.5}$ data	PM$_{2.5}$	µg/m^3	-	Hourly

[1] PBLH: Planetary boundary layer height. [2] SP: Surface pressure. [3] AT: Surface air temperature. [4] RH: Surface relative humidity. [5] WS: Surface wind speed.

2.2. Research Region

The BTH region includes 11 prefecture-level cities and two municipalities (Beijing and Tianjin) in Hebei Province. The region is China's northern economic hub as well as its political and cultural hub. The BTH region is topographically varied, including plains, hills, and mountains (Figure 2). The Yanshan Mountains and Taihang Mountains form its northern and western boundaries, respectively. These geographical conditions play a negative role in the dissipation of pollutants.

2.3. Methods

The workflow (Figure 3) of this study on estimating the nighttime PM$_{2.5}$ concentration in the BTH region involved data collection and processing, model construction, model

accuracy evaluation, and the final nighttime PM$_{2.5}$ concentration estimation (NightPMES) model in the BTH region.
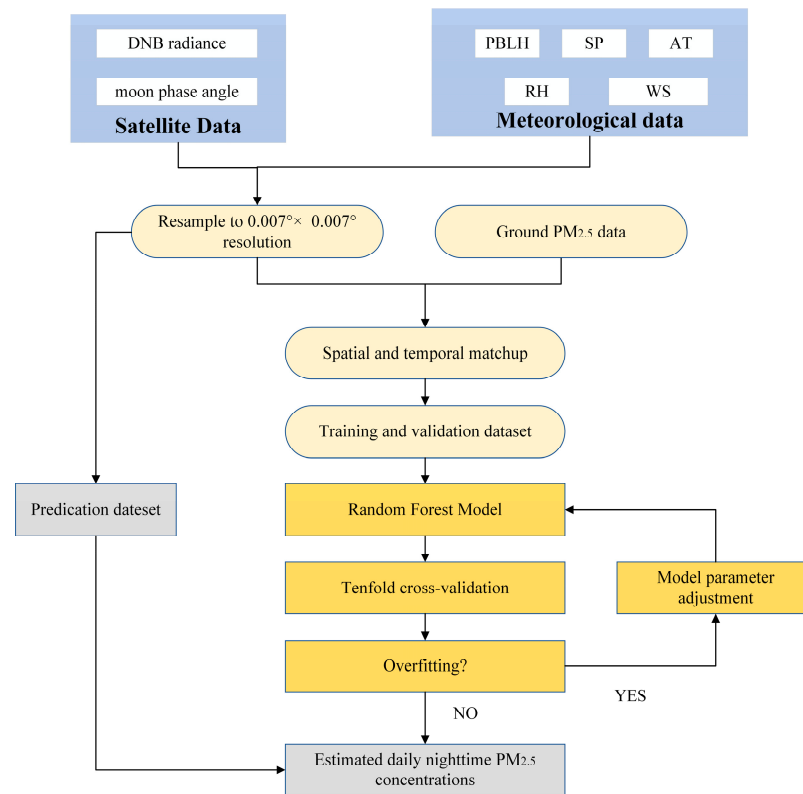
Figure 3. Flow chart of study procedure.

(1) Data collection and processing: The study used ground monitoring of PM$_{2.5}$ concentration, satellite, and meteorological (SP, PBLH, AT, RH, and WS) data. These data were preprocessed and spatiotemporally matched. Preprocessing involved geometric correction, cloud removal, cropping of satellite data, resampling and cutting of meteorological data, and removal of missing data (NAN) from the ground PM$_{2.5}$ data.

(2) Model building: The processed data set was trained with the random forest model, and the optimal parameters of the model were determined with the grid search. The grid search used the exhaustive method to search for the optimal parameters. The essence was to train the combination of all parameters and calculate the mean square error (MSE) of the corresponding model. Finally, the parameter combination with the minimum MSE was obtained, which was the optimal parameter combination of the model [35].

(3) Model accuracy evaluation: A 10-fold, cross-validation was performed. The model accuracy was evaluated with the RMSE, determination coefficient (R^2), and mean absolute error (MAE). The final NightPMES model was selected if it had sufficient precision; otherwise, the parameters were adjusted.

More specifically, the RMSE measures the deviation between estimated and true values, whereas R^2 is used in regression to assess the degree of compliance between estimated and true values. The MAE is calculated from the absolute value of the estimation error and can avoid mutual cancelation of errors. The formulas for RMSE, R^2, and MAE are expressed as Equations (1)–(3):

$$\mathrm{RMSE} = \sqrt{\frac{1}{m}\sum_{i=1}^{m}\left(\mathrm{PM}_{2.5\mathrm{true}} - \mathrm{PM}_{2.5\mathrm{estimate}}\right)^2} \tag{1}$$

$$R^2 = 1 - \frac{\sum_{i=1}^{m} \left(PM_{2.5true} - PM_{2.5estimate}\right)^2}{\sum_{i=1}^{m} \left(PM_{2.5true} - PM_{2.5average}\right)^2} \tag{2}$$

$$MAE = \frac{1}{m} \sum_{1}^{m} |PM_{2.5true} - PM_{2.5estimate}| \tag{3}$$

where $PM_{2.5true}$, $PM_{2.5estimate}$, and $PM_{2.5average}$ are the true, estimated, and average values of $PM_{2.5}$, respectively, while m is the total number of samples.

(4)　The estimation of the nighttime $PM_{2.5}$ concentration in the BTH region was performed by entering data (locations without surface $PM_{2.5}$ observations) into the NightPMES model.

2.3.1. NightPMES Model

The NightPMES model was based on a random forest, which adopts the idea of bagging and uses a decision tree as the base learner. A random feature selection is added to the random forest model to ensure that base learner diversity comes from more than sample perturbation. In a traditional decision tree, the optimal feature comes from the feature set of a given node. However, in a random forest, a subset with k features is randomly chosen from the traits of each node in the primary decision tree (where k controls the randomness of features). Subsequently, an optimal feature is selected from this subset for partitioning [36].

This study used the grid search method to determine the optimal parameters for the random forest model. When conducting the grid search, the n_estimators was set to 100–300, which was increased by 10 steps each time, and the max_depth was set to 20–50, which was increased by 1 step each time. Finally, after traversing all parameter combinations, the optimal parameters of the NightPMES model were the number of trees 240 and the maximum depth of trees 46 (Table 2). Therefore, the NightPMES model was fitted using Equation (4):

$$PM2.5 = f(\text{DNB radiance, moon phase angle, PBLH, SP, AT, RH, WS}) \tag{4}$$

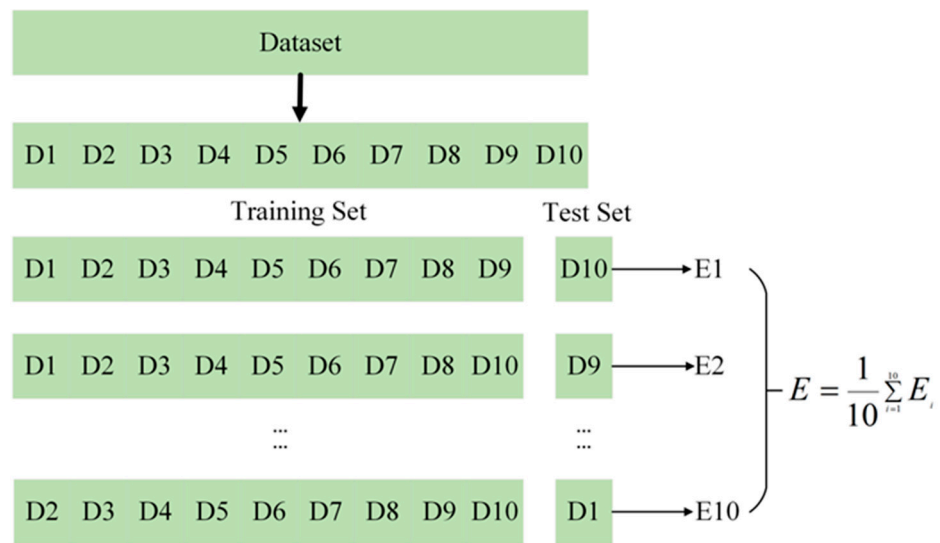**Table 2.** Optimal hyperparameters of the NightPMES model.

Parameter	Meaning	Value
n_estimators	Number of trees	240
max_depth	Maximum tree depth	46

The 10-fold, cross-validation method divided the dataset into 10 subsets (Figure 4). Each time, the nine subsets were pooled for use as the training set, and the remaining subset was the test set, yielding 10 sets of training/test combinations. The average of 10 test results was taken as the final result of the model [34].

2.3.2. Seasonal Model

The annual data were divided into four seasons to determine the seasonal variation of the nighttime $PM_{2.5}$ concentration. Spring included March, April, and May; summer included June, July, and August; autumn included September, October, and November; winter included December, January, and February. The sample sizes for the four seasons were 3324, 2156, 4327, and 3679, respectively. The seasonal models (Table 3) were trained using a random forest model.

**Figure 4.** Schematic of the 10-fold, cross-validation.

Table 3. Optimal hyperparameters for the seasonal models.

Season	Parameter	Value
Spring	n_estimators	100
	max_depth	20
Summer	n_estimators	100
	max_depth	20
Autumn	n_estimators	100
	max_depth	25
Winter	n_estimators	100
	max_depth	25

3. Results

3.1. Comparison of Different Models

Figure 5 shows a 10-fold, cross-validation scatterplot of the NightPMES model in the BTH region. After spatiotemporal matching, 13,486 samples were obtained. After model training, the R^2, RMSE, and MAE values were 0.82, 16.67, and 10.20, respectively. Thus, our NightPMES model performs well in the BTH region.
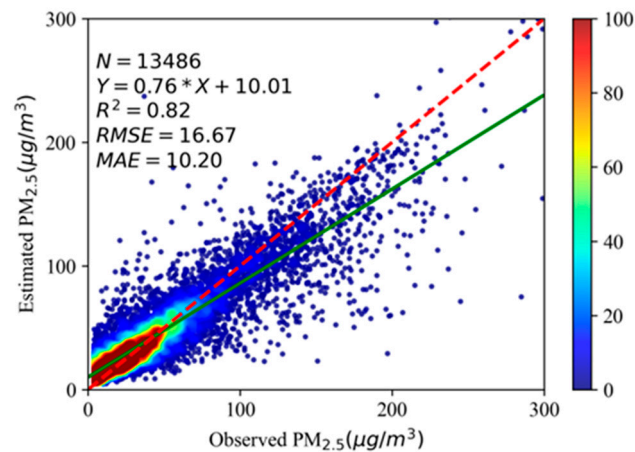
Figure 5. A 10-fold, cross-validation scatter plot of the NightPMES model in the BTH region. Green solid line: fitting line, and the red dotted line: 1:1 line.

To further assess model reliability, we compared the cross-validation results with the results from the MLR and deep neural networks (DNN). The former investigates the relationship between multiple independent variables and a dependent variable, resulting in a linear combination of multiple regression coefficients [37]. The DNN model (see parameters in Table 4) comprises input, hidden, and output layers. Each layer is completely connected, and the model is suitable for complex problems [38].

Table 4. Parameters of the DNN model.

Name	Value
Hidden layers number	4
Number of neurons	1024, 512, 256, 128
ActivationMethod	ReLU
Regularization	dropout
Number of iterations	1500
Loss function	MAE
Optimization functions	Adam
Initial learning rate	0.001

The MLR and DNN were constructed based on the VIIRS/DNB radiance, moon phase angle, and meteorological data. Equation (5) is the MLR function; Table 5 lists the model accuracy. The NightPMES model (R^2 = 0.82, RMSE = 16.67, and MAE = 10.20) performed better than the MLR (R^2 = 0.13, RMSE = 34.44, and MAE = 23.63) and DNN (R^2 = 0.74, RMSE = 20.18, and MAE = 12.46). Therefore, the NightPMES model was selected.

$$
\begin{aligned}
PM_{2.5MLR} &= 27.50 - 4.15\text{DNB radiance} - 21.04\text{PBLH} + 34.88\text{SP} - 30.50\text{WS} \\
&\quad -46.88\text{AT} + 27.50\text{RH}
\end{aligned}
\tag{5}
$$

Table 5. Comparison of various estimation models of PM$_{2.5}$ concentration in the BTH region at night.

| Model	R^2	RMSE ($\mu g/m^3$)	MAE ($\mu g/m^3$)
MLR	0.13	34.44	23.63
DNN	0.74	20.18	12.46
NightPMES	0.82	16.67	10.20

A comparison of the previous models with our NightPMES model indicated that the number of sites and samples we used was 6.7 times and 27.6 times higher than the greatest number of sites and samples from previous studies, respectively (Table 6). Additionally, the NightPMES model performed better than most other models (Table 6). Although the Support Vector Machine (SVM) and BP models have higher R^2 (0.9 and 0.83, respectively), they each contained only 50 and 198 samples. However, the NightPMES model maintained high accuracy even with a large number of samples. Overall, the NightPMES model performed better and was more reliable.

### 3.2. Temporal and Spatial Distribution of Nighttime PM$_{2.5}$ Concentration

To better observe the seasonal variation in the nighttime PM$_{2.5}$ concentration, we analyzed the PM$_{2.5}$ concentrations in the BTH region throughout 2021. The nighttime PM$_{2.5}$ concentration was highest in winter followed by spring and autumn, with the lowest values during summer (Figure 6a–d). The southern Yanshan and Taihang Mountains had higher PM$_{2.5}$ concentrations than that of the northern mountainous area (Figure 6a,c,d), consistent with elevation (Figure 2). In addition, the NightPMES model estimated seasonal mean corresponded with the observed seasonal mean from the ground stations in their spatial distribution (Figure 6a–h). The seasonal average of the estimated PM$_{2.5}$ concentrations were strongly correlated with the ground observations (Figure 6i–l) with R^2 for spring, summer, autumn, and winter being 0.98, 0.92, 0.95, and 0.95, respectively.

Table 6. Statistics of the models for estimating the nighttime PM$_{2.5}$ concentration based on the VIIRS/DNB data.

Model	Number of Sites	Sample Size	R^2	RMSE (μg/m^3)	Reference
MLR	5	75	0.45	4.114	Wang et al. (2016) [26]
SVM	4	50	0.90	-	Zhao et al. (2017) [39]
BP	12	198	0.83	14.02	Zhao et al. (2016) [27]
MLR	9	488	0.77	19.21	Li et al. (2019) [40]
SVM	18	324	0.77	32.05	Chen et al. (2022) [41]
NightPMES	121	13486	0.82	16.67	This study
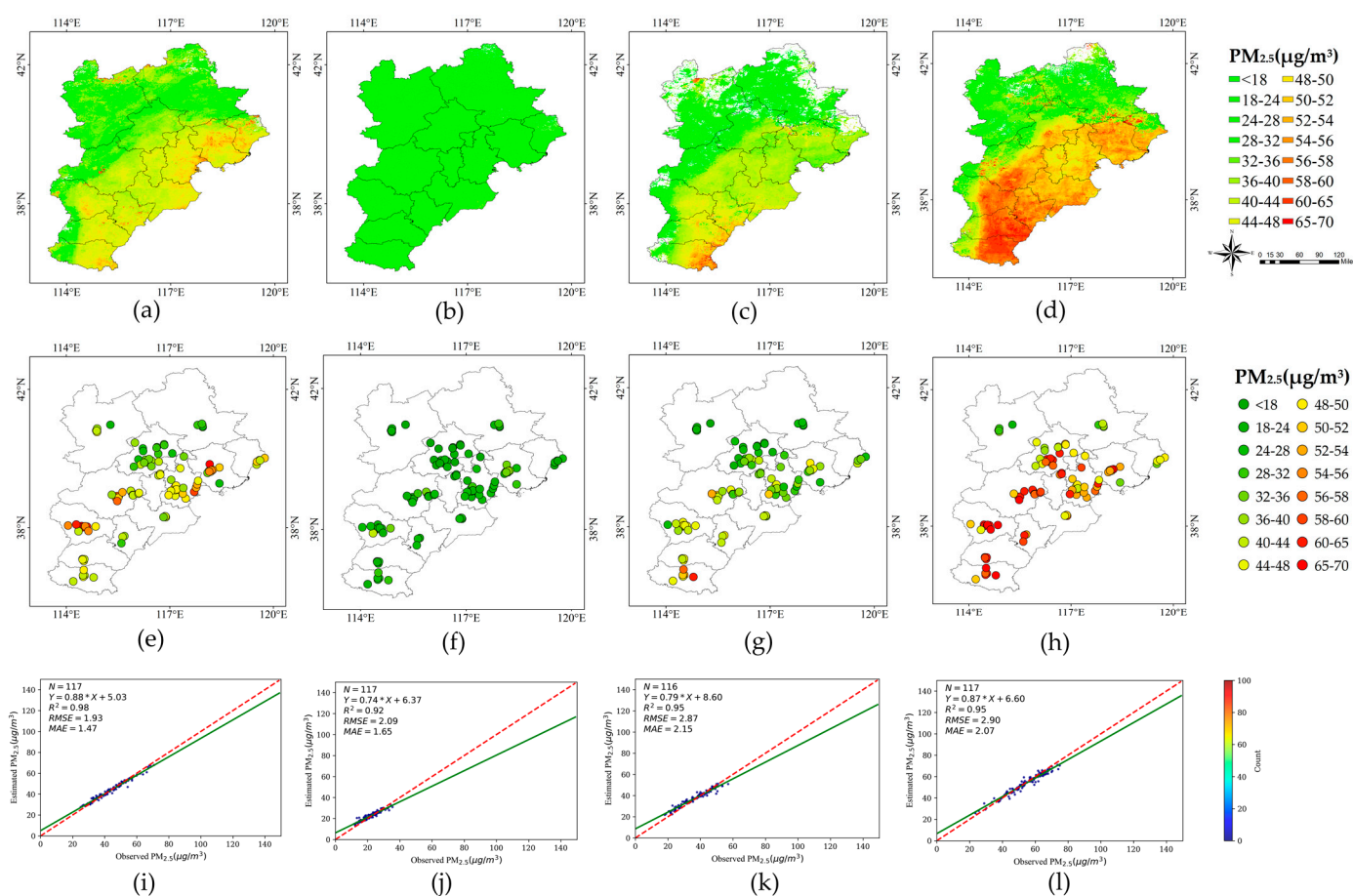
Figure 6. Spatial distributions for spring (March, April, and May), summer (June, July, and August), autumn (September, October, and November), and winter (December, January, and February) mean PM$_{2.5}$ concentrations. (**a**–**d**) NightPMES model estimates; (**e**–**h**) ground observations; (**i**–**l**) scatterplots of the ground observations versus the NightPMES model estimates.

The average annual PM$_{2.5}$ concentration was low in the northwest and high in the southeast (Figure 7). The southern plains of the BTH region had relatively high PM$_{2.5}$ concentrations, likely because of the numerous industrial factories in that area. Chengde and Zhangjiakou in the northwest are covered with more vegetation, conducive to lowering the PM$_{2.5}$ concentration. The scatter plot of the annual average observed versus the estimated PM$_{2.5}$ concentrations shows a strong relationship with R^2, RMSE, and MAE of 0.96, 1.95, and 1.5, respectively (Figure 7c).
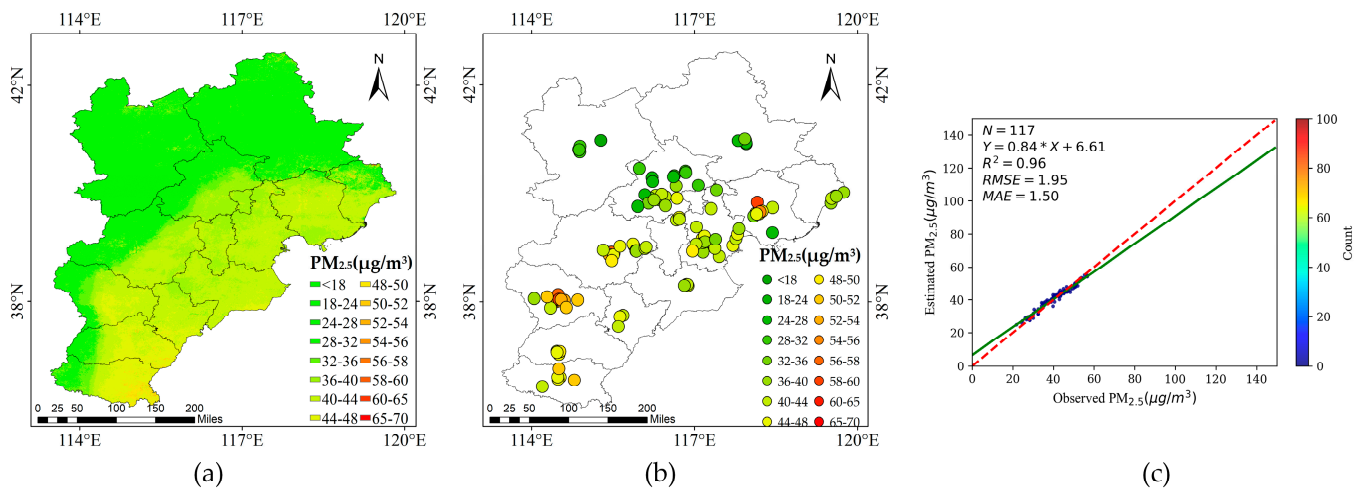
Figure 7. Spatial distributions of the annual average PM$_{2.5}$ concentrations. (**a**) NightPMES model estimates; (**b**) ground observations; (**c**) scatterplot of the ground observations versus the NightPMES model estimates.

3.3. Effect of Moon Phase Angle on Nighttime PM$_{2.5}$ Concentration

The primary sources of visible light at night are moonlight and ground light. Moonlight is a highly variable quantity because the moon itself is not a self-luminous object; it just reflects the sunlight incident on it. The illumination of the moon from earth is variable throughout the lunar cycle. Ground light sources have relatively stable intensity over a given period, and its radiation is at least 10-times the intensity of moonlight [21]. The vector angle between the sun–moon and earth–moon is known as the moon phase angle. Therefore, to limit the influence of moonlight, researchers typically use only data with a moon phase angle greater than 120°. However, this also leads to much less valid data available at night.

Here, we constructed models using data with the moon phase angle >120° and ≤120°. Figure 8 shows a diagram of the 10-fold, cross-validation results of the two models. The trained model using 4217 samples with a moon phase angle >120° had an R^2 of 0.84, RMSE of 19.843, and MAE of 11.45 (Figure 8a). The model using 9269 samples with a moon phase angle < 120° had an R^2 of 0.79, RMSE of 14.87, and MAE of 9.50 (Figure 8b). The R^2 for >120° data was only 0.02 higher than the NightPMES model (Figures 5 and 8a), while the available time decreased by approximately 60% (Figure 9).
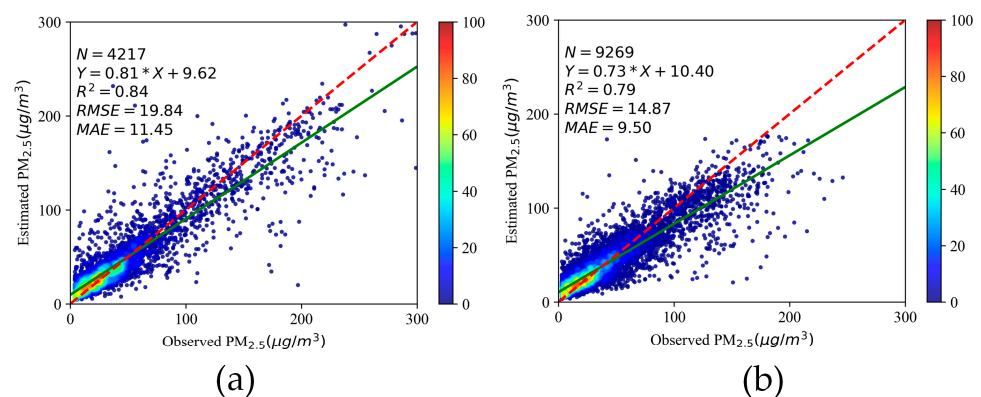
Figure 8. Scatterplots of the RF model with 10-fold, cross-validation of model accuracy. Data with (**a**) moon phase angle > 120° and with (**b**) moon phase angle ≤ 120°. Red dashed line, 1:1 line; solid green line, fitted line.
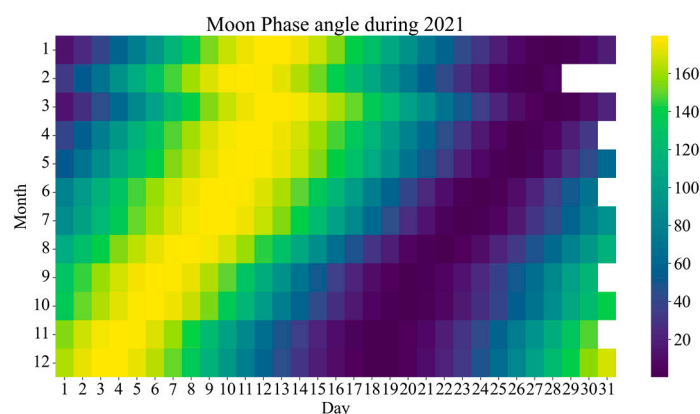
Figure 9. Daily moon phase angle during 2021.

Every day, NPP/VIIRS passes the BTH region at approximately 2:00 a.m. Beijing Time. Figure 9 shows the daily moon phase angle at 18:00 (Universal Time Coordinated, UTC) during 2021. The number of days with a moon phase angle > 120° accounts for approximately 40% of the entire year (Figure 9), meaning that a model excluding ≤ 120° data can only estimate approximately 140 days of data per year and 11 days of data per month. Our analyses suggest that the NightPMES model can effectively estimate $PM_{2.5}$ concentration despite being constructed from observations at all moon phase angles, which greatly enhances the model's applicability.

3.4. Effect of Seasonal Characteristics on Nighttime $PM_{2.5}$ Concentration

The seasonal model (Section 2.3.2) had higher accuracy during spring and autumn than the NightPMES model (Figure 10). The R^2, RMSE, and MAE for the spring model were 0.83, 15.99, and 9.92, respectively, whereas the corresponding values for the autumn model were 0.83, 13.38, and 8.74. Thus, the two seasonal models yielded a higher R^2 and lower RMSE and MAE than the NightPMES model (0.82, 16.67, and 10.20). The R^2, RMSE, and MAE of the winter model were 0.86, 18.07, and 11.50, respectively. Although the R^2 of the winter model was higher than that of the NightPMES model, the RMSE and MAE were larger than those of the NightPMES model. The range of wintertime $PM_{2.5}$ values was 0–300 μg/m^3 with numerous observations being close to the upper limit (Figure 10d). In addition, the winter heating season is often accompanied by increased sulfur dioxide and particulate matter emissions into the atmosphere, resulting in high $PM_{2.5}$ concentra-tions. The frequent occurrence of high concentrations of $PM_{2.5}$ may be the reason for the large RMSE and MAE of the winter model.

The performances of the summer and NightPMES models were quite different. The R^2 value of the summer model was only 0.58. The following are the possible reasons for the poor accuracy of the summer model: First, more frequent rainfall in summer is conducive to the settlement of $PM_{2.5}$, while the summer model does not include the factor of precipitation; second, the higher vegetation coverage rate in summer can effectively reduce the concentration of $PM_{2.5}$ and affect the upward radiation of ground lights. Here, we use the Normalized Difference Vegetation Index (NDVI) to characterize vegetation cover. The MODIS 1 km NDVI monthly data (MOD13A3) was downloaded from https://doi.org/10.5067/MODIS/MOD13A3.006, accessed on 6 May 2022. The NDVI in Figure 11 is the monthly average of the BTH region. Figure 11 shows that the trends for NDVI and DNB over time is opposite. The NDVI increases monthly, reaches a maximum in August, and then decreases continuously. The DNB showed an opposite trend. The dense vegetation in summer blocks ground light and affects the upward radiation of the ground light source, which weakens the radiation reaching the DNB imager.
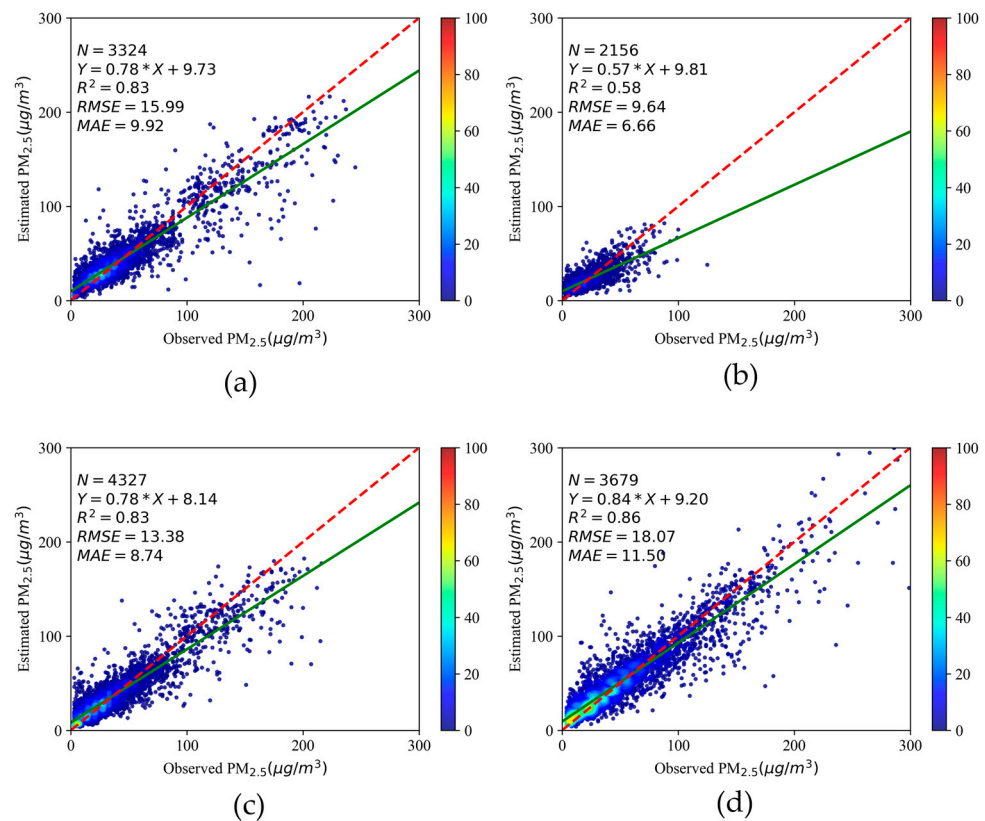
Figure 10. Seasonal model 10-fold, cross-validation scatterplots for the estimated PM$_{2.5}$ concentration in 2021. (**a**) Spring; (**b**) Summer; (**c**) Autumn; (**d**) Winter. Red dashed line, 1:1 line; green line, fitted line.
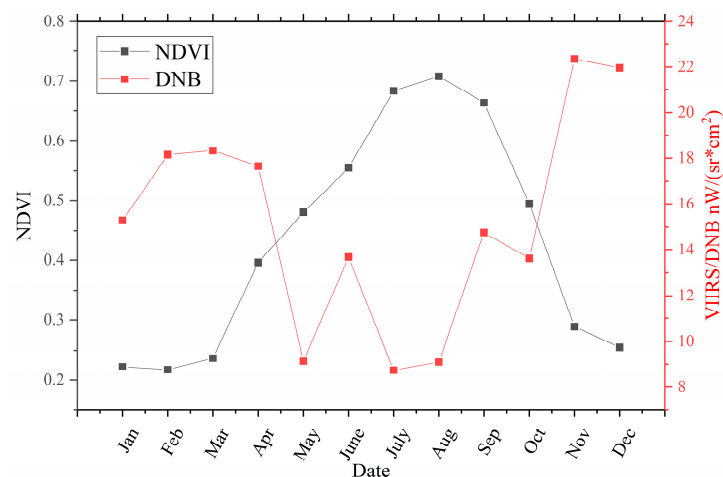

Figure 11. Monthly variations of NDVI and VIIRS/DNB radiance in BTH 2021.

### 3.5. Analysis of the Diurnal Variation of PM$_{2.5}$ Concentration

Combining both the daytime and nighttime monitoring data is useful for describing the diurnal variation in PM$_{2.5}$ concentration. Figure 12 shows the variation of PM$_{2.5}$ concentration in the four seasons and its standard deviation (longitude: 114.5481°, latitude: 38.0378°) in 2021. As solar radiation increased from 7:00 to 14:00 (Beijing Time), the PM$_{2.5}$ concentration decreased. The lowest concentration occurred at approximately 15:00 (Beijing Time), then gradually increased from 16:00 to 20:00 (Beijing Time), reflecting the increase in road traffic and vehicle exhaust emissions along with the weakening of boundary layer turbulence at night. A small peak appeared at approximately 21:00 (Beijing Time),

then remained relatively stable from 22:00 to 5:00 (Beijing Time), reflecting the stability in the atmospheric boundary layer at night. The R^2 between the PM$_{2.5}$ concentration at the VIIRS overpass time and the average daily PM$_{2.5}$ concentration reached 0.77, indicating that the two variables were strongly correlated (Figure 13). Therefore, VIIRS/DNB-based nighttime PM$_{2.5}$ concentrations reflect the PM$_{2.5}$ concentration at the time of satellite overpass and approximate daily average PM$_{2.5}$ concentration. Our results indicate that satellite data can be an important supplement when monitoring PM$_{2.5}$ variation.
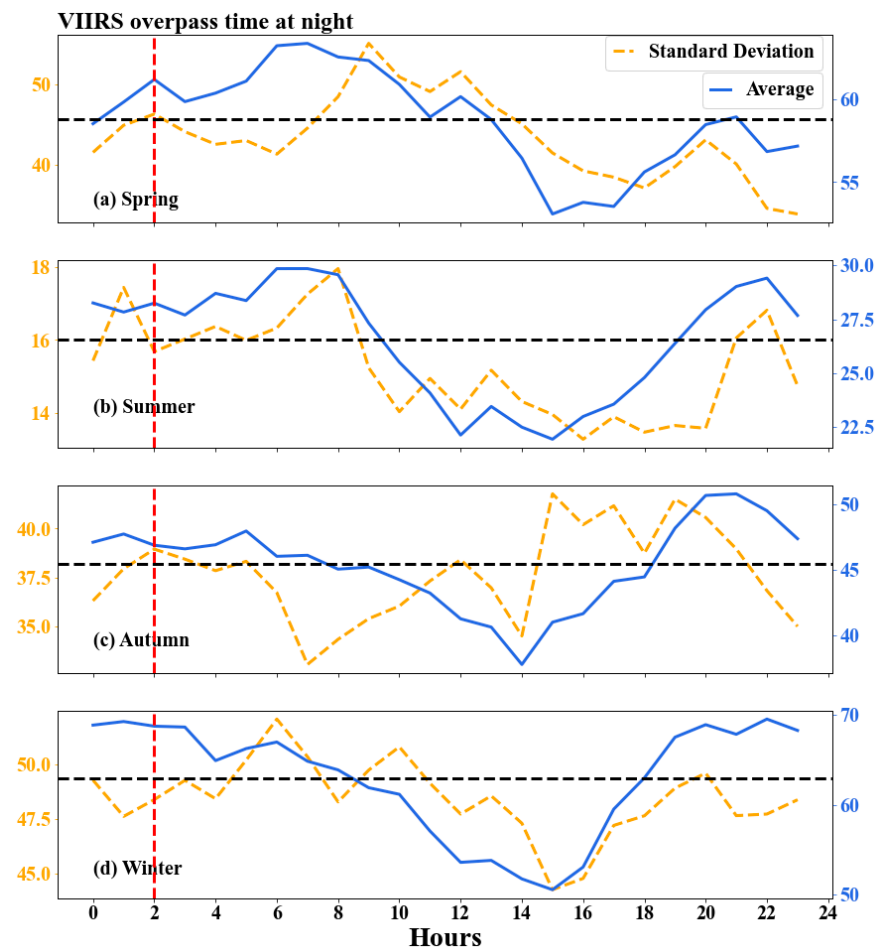

Figure 12. Hourly seasonal average of PM$_{2.5}$ concentration at the Shijiazhuang site (longitude: 114.5481°, latitude: 38.0378°) in Beijing Time. The orange dotted line represents the hourly standard deviation of the seasonal average. The blue solid line represents the hourly PM$_{2.5}$ concentration of the seasonal average. The red dotted line represents the PM$_{2.5}$ concentration at the time of the VIIRS overpass, while the black dotted line is the seasonal average daily PM$_{2.5}$ concentration (right y axis).

We observed that the PM$_{2.5}$ concentration changes significantly during the day (7:00–20:00, Beijing Time) but not during the night (21:00–6:00, Beijing Time) (Figure 12). Pollutants are challenging to diffuse at night because the boundary layer is more stable and temperature inversions are frequent. Figure 14 shows the temperature inversion intensity at different times. The intensity of the temperature inversion was greater at 2:00 (Beijing Time) but then decreased gradually as the solar radiation increased (Figure 14) [42]. With sunrising, the ground warms up and temperature inversions slowly dissipate, leading to gradual changes in the PM$_{2.5}$ concentration. Thus, temperature inversions are a reason for the large difference in the PM$_{2.5}$ concentration between day and night.
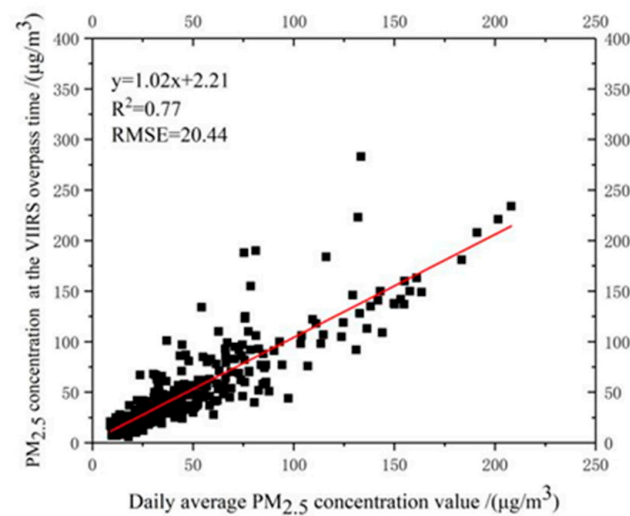
Figure 13. Scatter plot of PM$_{2.5}$ concentration at 2:00 (UTC) and the daily average. Fitted line is in red.
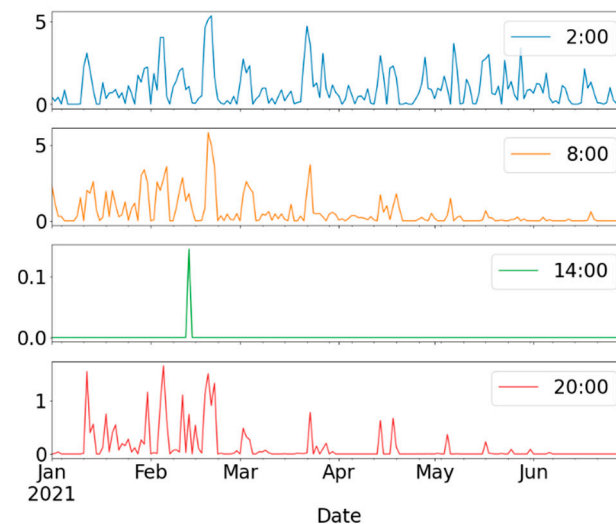
Figure 14. Six-hourly temperature inversion intensity of the Shijiazhuang site from January to June 2021 in Beijing Time.

Figure 15 shows the diurnal variation of pollution. The estimated daytime PM$_{2.5}$ concentrations come from the ChinaHighPM$_{2.5}$ dataset [11,43,44]. On 8 March, the northwest BTH region was moderately polluted (PM$_{2.5}$ between 115 and 150), while the other areas were slightly polluted (PM$_{2.5}$ between 75 and 115) (Figure 15d). By the early hours of 9 March (Figure 15e), southern Zhangjiakou, eastern Beijing, Tianjin, as well as central and eastern Hebei gradually became moderately polluted. On 9 March (Figure 15f), Beijing, Tianjin, and most parts of eastern and central Hebei were heavily polluted (PM$_{2.5}$ greater than 150). In addition, the estimated PM$_{2.5}$ concentrations were consistent with the spatial distribution of the PM$_{2.5}$ concentrations from the ground stations (Figure 15d–i). The diurnal trends of the PM$_{2.5}$ concentration indicate that heavy pollution varied clearly during the day (Figure 15). It indicated that combining the estimates of the nighttime PM$_{2.5}$ concentration estimations would benefit a more nuanced understanding of the spatial and temporal variations in air pollution.
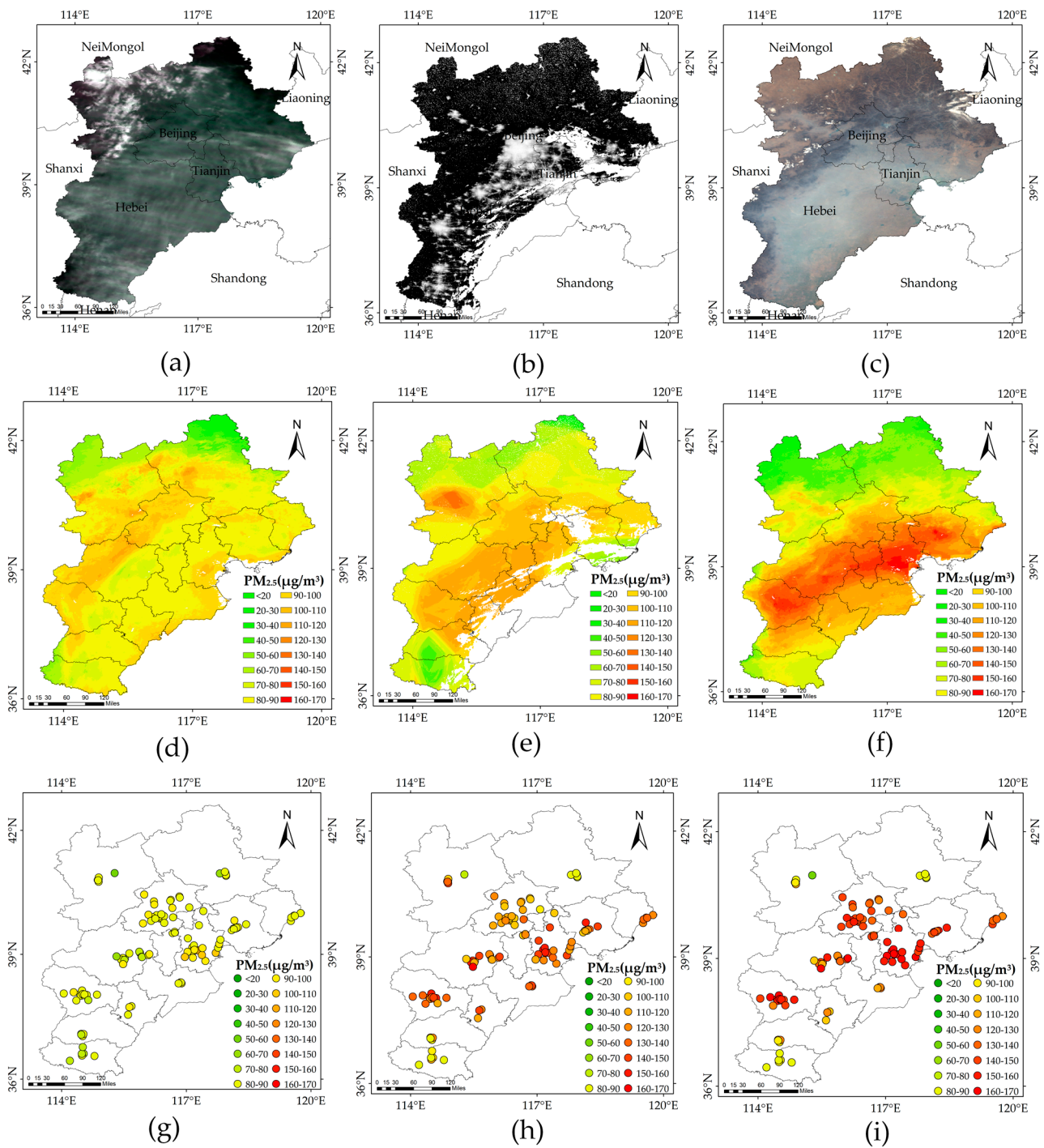
Figure 15. Diurnal variation of pollution in the BTH region based on satellite remote sensing images. (**a**) True color image of MODIS on 8 March 2021 (03:50 UTC); (**b**) Cloud-masked VIIRS/DNB radiance on 8 March 2021 (17:32 UTC); (**c**) True color image of MODIS on 9 March 2021 (02:55 UTC); (**d**–**f**) Plots of $PM_{2.5}$ concentration estimations corresponding to (**a**–**c**); (**g**–**i**) Plots of $PM_{2.5}$ concentration observations at ground stations corresponding to (**a**–**c**).

4. Discussion

This study estimated the nighttime $PM_{2.5}$ concentrations in the BTH region during 2021 using a combination of VIIRS/DNB radiance and $PM_{2.5}$ concentration data from ground stations. Based on the VIIRS/DNB radiance and moon phase angles combined with meteorological factors (SP, PBLH, AT, RH, and WS) as independent variables, we established several $PM_{2.5}$ concentration estimation models, including the NightPMES,

MLR, and DNN. Our results show that the NightPMES model performed significantly better than the MLR or DNN models. The NightPMES model had an R^2, RMSE, and MAE of 0.82, 16.67, and 10.20, respectively. Additionally, the NightPMES model had better performance than most previous models (Table 5). The nighttime $PM_{2.5}$ concentration obtained with this model effectively characterized the spatial patterns of the nighttime atmosphere in the BTH region. Moreover, we obtained more information to monitor the nighttime atmospheric environment.

The possible errors of the proposed NightPMES model were analyzed. First, this study used the threshold method to remove clouds, and there may be residual cloud pixels, especially for thin clouds, as the reflectivity of clouds is usually higher than the surface, and its transmittance is lower than $PM_{2.5}$. The residual cloud pixels will enhance the reflection of moonlight radiation when there is moonlight, while it will reduce the upward radiation of ground light when there is only ground light. Therefore, it will be mistaken for the contribution of $PM_{2.5}$. Second, there are obvious spatial differences between the ground observation and satellite observation. Usually, the ground observation represents a single point, while the satellite observation is the average of a certain range (spatial resolution of 750 m). Therefore, there will be a smooth effect, which leads to the overestimation of $PM_{2.5}$ when the concentration is low. Third, the spatial resolution of the meteorological factors used in this study is coarse ($0.5° \times 0.625°$), resulting in the spatial variation of the meteorological factors being smoothed. The meteorological data with smooth spatial changes also have a mean effect, which leads to errors in the $PM_{2.5}$ concentration estimation.

Various complex relationship models for estimating the nighttime $PM_{2.5}$ concentration can be obtained via combining satellite data with different base models. A model that ignored the influence of moonlight (including only data with phase angle > 120°) performed better than the NightPMES model (Figure 8). This outcome indicates that the estimation model of nighttime $PM_{2.5}$ concentration is sensitive to lunar illumination. The moon phase angle magnitude reflects the influence of lunar radiation; therefore, a lunar irradiance model is necessary for quantifying this influence in subsequent research [45,46].

There were four distinct seasons in the BTH region, and we observed clear spatiotemporal variations to the nighttime $PM_{2.5}$ concentrations (Figure 6). Seasonally, winter saw greater $PM_{2.5}$ concentrations, whereas summer saw lower levels. Spatially, Handan, Xingtai, and Shijiazhuang in the southeast had higher concentrations, whereas Zhangjiakou and Chengde in the northwest had lower concentrations. With our seasonal model, we analyzed the influence of the seasonality of the nighttime $PM_{2.5}$ concentration in summer and winter, providing a reference for further research. Additionally, based on the analysis of daytime and nighttime $PM_{2.5}$ concentrations, we found that $PM_{2.5}$ pollution can be better understood if nighttime data are included. Overall, the NightPMES model provides a reliable estimation of the nighttime $PM_{2.5}$ concentration in the BTH region and should help improve $PM_{2.5}$ monitoring efforts.

Although this study proposed a better model for nighttime $PM_{2.5}$ concentration monitoring, it has several limitations. The NightPMES model was only tested in the BTH region, so to validate it further, studies with larger spatial scales and extended time series are needed. In addition, although we included several variables that may influence nighttime $PM_{2.5}$ concentration, we did not consider many other factors, such as NDVI, precipitation, elevation, population, and economy. Adding more variables into our model will possibly increase the estimation accuracy. Furthermore, we mainly concentrated on urban areas, thus limiting model applicability. Increasing the number of suburban sites in future research will address this issue. Finally, the VIIRS/DNB measures of nighttime radiation mainly originate from moonlight and ground light. Therefore, the contribution of moonlight must be quantified. To optimize the monitoring and estimation of nighttime $PM_{2.5}$ concentration, a moon irradiance model can be introduced into the NightPMES model.

Satellites equipped with low-light sensors, such as FY-3E and the Sustainable Development Science Satellite 1 (SDGSAT-1), have been launched recently. These sensors

have higher temporal and radiation resolution, providing an excellent opportunity for monitoring the nighttime atmospheric environment.

5. Conclusions

Here, we generated a NightPMES model for estimating the nighttime $PM_{2.5}$ concentration in the BTH region using DNB radiance, meteorological elements, and moon phase angle. After experimental verification, we arrived at four conclusions.

First, the NightPMES model (R^2 = 0.82, RMSE = 16.67, and MAE = 10.20) performed better than the MLR or DNN models.

Second, when all moon phase angles were included, we increased the available data by approximately 60% from previous studies. Hence, the NightPMES model was capable of obtaining daily estimations for $PM_{2.5}$ concentration.

Third, significant seasonal differences in the nighttime $PM_{2.5}$ concentrations are explained by the seasonal characteristics of DNB radiation (highest in winter and lowest in summer), along with obvious seasonal meteorological conditions.

Fourth, the dynamics of $PM_{2.5}$ concentration can be analyzed more accurately when the nighttime $PM_{2.5}$ concentration (estimated by the NightPMES model) is combined with the daytime $PM_{2.5}$ concentration.

To conclude, pollution monitoring should take advantage of the many satellites equipped with low-light imagers that have been or will be launched. This study validates the use of low-light remote sensing data to estimate nighttime $PM_{2.5}$ concentration and provides a basis for applying satellite data to nighttime atmospheric environmental monitoring.

Author Contributions: The authors' contributions are as follows: conceptualization, methodology, validation, formal analysis, and data curation, Y.M. and W.Z.; writing-original draft preparation, Y.M.; writing-review and editing, all authors; supervision, L.Z.; and funding acquisition, W.Z.; and project administration, X.G. and T.Y. All authors have read and agreed to the published version of the manuscript.

Conflicts of Interest: The authors declare no conflict of interest.

References

1. Zhang, D.; Du, L.; Wang, W.; Zhu, Q.; Bi, J.; Scovronick, N.; Naidoo, M.; Garland, R.M.; Liu, Y. A Machine Learning Model to Estimate Ambient $PM_{2.5}$ Concentrations in Industrialized Highveld Region of South Africa. *Remote Sens. Environ.* **2021**, *266*, 112713. [CrossRef]
2. World Health Organization. *WHO Global Air Quality Guidelines: Particulate Matter (PM2.5 and PM10), Ozone, Nitrogen Dioxide, Sulfur Dioxide and Carbon Monoxide*; World Health Organization: Geneva, Switzerland, 2021.
3. Xie, R.; Sabel, C.E.; Lu, X.; Zhu, W.; Kan, H.; Nielsen, C.P.; Wang, H. Long-Term Trend and Spatial Pattern of $PM_{2.5}$ Induced Premature Mortality in China. *Environ. Int.* **2016**, *97*, 180–186. [CrossRef] [PubMed]
4. Vodonos, A.; Awad, Y.A.; Schwartz, J. The Concentration-Response between Long-Term PM 2.5 Exposure and Mortality; A Meta-Regression Approach. *Environ. Res.* **2018**, *166*, 677–689. [CrossRef] [PubMed]
5. Mousavi, S.E.; Amini, H.; Heydarpour, P.; Amini Chermahini, F.; Godderis, L. Air Pollution, Environmental Chemicals, and Smoking May Trigger Vitamin D Deficiency: Evidence and Potential Mechanisms. *Environ. Int.* **2019**, *122*, 67–90. [CrossRef] [PubMed]
6. Amini, H.; Trang Nhung, N.T.; Schindler, C.; Yunesian, M.; Hosseini, V.; Shamsipour, M.; Hassanvand, M.S.; Mohammadi, Y.; Farzadfar, F.; Vicedo-Cabrera, A.M.; et al. Short-Term Associations between Daily Mortality and Ambient Particulate Matter, Nitrogen Dioxide, and the Air Quality Index in a Middle Eastern Megacity. *Environ. Pollut.* **2019**, *254*, 113121. [CrossRef]
7. Coleman, C.J.; Yeager, R.A.; Pond, Z.A.; Riggs, D.W.; Bhatnagar, A.; Arden Pope, C. Mortality Risk Associated with Greenness, Air Pollution, and Physical Activity in a Representative U.S. Cohort. *Sci. Total Environ.* **2022**, *824*, 153848. [CrossRef]

8. Zhang, L.; Wilson, J.P.; MacDonald, B.; Zhang, W.; Yu, T. The Changing PM$_{2.5}$ Dynamics of Global Megacities Based on Long-Term Remotely Sensed Observations. *Environ. Int.* **2020**, *142*, 105862. [CrossRef]

9. Weichenthal, S.; Pinault, L.; Christidis, T.; Burnett, R.T.; Brook, J.R.; Chu, Y.; Crouse, D.L.; Erickson, A.C.; Hystad, P.; Li, C.; et al. How Low Can You Go? Air Pollution Affects Mortality at Very Low Levels. *Sci. Adv.* **2022**, *8*, eabo3381. [CrossRef]

10. Peng, J.; Han, H.; Yi, Y.; Huang, H.; Xie, L. Machine Learning and Deep Learning Modeling and Simulation for Predicting PM$_{2.5}$ Concentrations. *Chemosphere* **2022**, *308*, 136353. [CrossRef] [PubMed]

11. Wei, J.; Li, Z.; Lyapustin, A.; Sun, L.; Peng, Y.; Xue, W.; Su, T.; Cribb, M. Reconstructing 1-Km-Resolution High-Quality PM$_{2.5}$ Data Records from 2000 to 2018 in China: Spatiotemporal Variations and Policy Implications. *Remote Sens. Environ.* **2021**, *252*, 112136. [CrossRef]

12. Zhang, L.; Wilson, J.P.; Zhao, N.; Zhang, W.; Wu, Y. The Dynamics of Cardiovascular and Respiratory Deaths Attributed to Long-Term PM$_{2.5}$ Exposures in Global Megacities. *Sci. Total Environ.* **2022**, *842*, 156951. [CrossRef] [PubMed]

13. Zhang, W.; Zheng, F.; Zhang, W.; Yang, X. Estimating Ground-Level Hourly PM$_{2.5}$ Concentrations Over North China Plain with Deep Neural Networks. *J. Indian Soc. Remote Sens.* **2021**, *49*, 1839–1852. [CrossRef]

14. Li, R.; Liu, X.; Li, X. Estimation of the PM$_{2.5}$ Pollution Levels in Beijing Based on Nighttime Light Data from the Defense Meteorological Satellite Program-Operational Linescan System. *Atmosphere* **2015**, *6*, 607–622. [CrossRef]

15. Chen, G.; Li, S.; Knibbs, L.D.; Hamm, N.A.S.; Cao, W.; Li, T.; Guo, J.; Ren, H.; Abramson, M.J.; Guo, Y. A Machine Learning Method to Estimate PM$_{2.5}$ Concentrations across China with Remote Sensing, Meteorological and Land Use Information. *Sci. Total Environ.* **2018**, *636*, 52–60. [CrossRef] [PubMed]

16. Ma, Z.; Dey, S.; Christopher, S.; Liu, R.; Bi, J.; Balyan, P.; Liu, Y. A Review of Statistical Methods Used for Developing Large-Scale and Long-Term PM$_{2.5}$ Models from Satellite Data. *Remote Sens. Environ.* **2022**, *269*, 112827. [CrossRef]

17. Hidy, G.M.; Brook, J.R.; Chow, J.C.; Green, M.; Husar, R.B.; Lee, C.; Scheffe, R.D.; Swanson, A.; Watson, J.G. Remote Sensing of Particulate Pollution from Space: Have We Reached the Promised Land? *J. Air Waste Manag. Assoc.* **2009**, *59*, 1130–1139. [CrossRef] [PubMed]

18. Li, S.; Joseph, E.; Min, Q. Remote Sensing of Ground-Level PM$_{2.5}$ Combining AOD and Backscattering Profile. *Remote Sens. Environ.* **2016**, *183*, 120–128. [CrossRef]

19. Yazdi, M.D.; Kuang, Z.; Dimakopoulou, K.; Barratt, B.; Suel, E.; Amini, H.; Lyapustin, A.; Katsouyanni, K.; Schwartz, J. Predicting Fine Particulate Matter (PM$_{2.5}$) in the Greater London Area: An Ensemble Approach Using Machine Learning Methods. *Remote Sens.* **2020**, *12*, 914. [CrossRef]

20. Feng, Y.; Fan, S.; Xia, K.; Wang, L. Estimation of Regional Ground-Level PM$_{2.5}$ Concentrations Directly from Satellite Top-of-Atmosphere Reflectance Using A Hybrid Learning Model. *Remote Sens.* **2022**, *14*, 2714. [CrossRef]

21. Miller, S.D.; Turner, R.E. A Dynamic Lunar Spectral Irradiance Data Set for NPOESS/VIIRS Day/Night Band Nighttime Environmental Applications. *IEEE Trans. Geosci. Remote Sens.* **2009**, *47*, 2316–2329. [CrossRef]

22. Cao, C.; De Luccia, F.J.; Xiong, X.; Wolfe, R.; Weng, F. Early On-Orbit Performance of the Visible Infrared Imaging Radiometer Suite Onboard the Suomi National Polar-Orbiting Partnership (S-NPP) Satellite. *IEEE Trans. Geosci. Remote Sens.* **2014**, *52*, 1142–1156. [CrossRef]

23. Johnson, R.S.; Zhang, J.; Hyer, E.J.; Miller, S.D.; Reid, J.S. Preliminary Investigations toward Nighttime Aerosol Optical Depth Retrievals from the VIIRS Day/Night Band. *Atmos. Meas. Tech.* **2013**, *6*, 1245–1255. [CrossRef]

24. McHardy, T.M.; Zhang, J.; Reid, J.S.; Miller, S.D.; Hyer, E.J.; Kuehn, R.E. An Improved Method for Retrieving Nighttime Aerosol Optical Thickness from the VIIRS Day/Night Band. *Atmos. Meas. Tech.* **2015**, *8*, 4773–4783. [CrossRef]

25. Zhang, J.; Jaker, S.L.; Reid, J.S.; Miller, S.D.; Solbrig, J.; Toth, T.D. Characterization and Application of Artificial Light Sources for Nighttime Aerosol Optical Depth Retrievals Using the Visible Infrared Imager Radiometer Suite Day/Night Band. *Atmos. Meas. Tech.* **2019**, *12*, 3209–3222. [CrossRef]

26. Wang, J.; Aegerter, C.; Xu, X.; Szykman, J.J. Potential Application of VIIRS Day/Night Band for Monitoring Nighttime Surface PM$_{2.5}$ Air Quality from Space. *Atmos. Environ.* **2016**, *124*, 55–63. [CrossRef]

27. Zhao, X.; Shi, H.; Yu, H.; Yang, P. Inversion of Nighttime PM$_{2.5}$ Mass Concentration in Beijing Based on the VIIRS Day-Night Band. *Atmosphere* **2016**, *7*, 136. [CrossRef]

28. Fu, D.; Xia, X.; Duan, M.; Zhang, X.; Li, X.; Wang, J.; Liu, J. Mapping Nighttime PM$_{2.5}$ from VIIRS DNB Using a Linear Mixed-Effect Model. *Atmos. Environ.* **2018**, *178*, 214–222. [CrossRef]

29. Erkin, N.; Simayi, M.; Ablat, X.; Yahefu, P.; Maimaiti, B. Predicting Spatiotemporal Variations of PM$_{2.5}$ Concentrations during Spring Festival for County-Level Cities in China Using VIIRS-DNB Data. *Atmos. Environ.* **2022**, *294*, 119484. [CrossRef]

30. Wu, J.; Yao, F.; Li, W.; Si, M. VIIRS-Based Remote Sensing Estimation of Ground-Level PM$_{2.5}$ Concentrations in Beijing–Tianjin–Hebei: A Spatiotemporal Statistical Model. *Remote Sens. Environ.* **2016**, *184*, 316–328. [CrossRef]

31. Hu, S.; Ma, S.; Yan, W.; Jiang, J.; Huang, Y. A New Multichannel Threshold Algorithm Based on Radiative Transfer Characteristics for Detecting Fog/Low Stratus Using Night-Time NPP/VIIRS Data. *Int. J. Remote Sens.* **2017**, *38*, 5919–5933. [CrossRef]

32. Liao, L.B.; Weiss, S.; Mills, S.; Hauss, B. Suomi NPP VIIRS Day-Night Band on-Orbit Performance. *J. Geophys. Res. Atmos.* **2013**, *118*, 12705–12718. [CrossRef]

33. Xia, L.; Mao, K.; Sun, Z.; Ma, Y. Introduction of Suomi NPP VIIRS and Its Application on Cloud Detection. *Adv. Geosci* **2013**, *3*, 6. [CrossRef]

34. Ali, M.A.; Bilal, M.; Wang, Y.; Nichol, J.E.; Mhawish, A.; Qiu, Z.; de Leeuw, G.; Zhang, Y.; Zhan, Y.; Liao, K.; et al. Accuracy Assessment of CAMS and MERRA-2 Reanalysis $PM_{2.5}$ and PM_{10} Concentrations over China. *Atmos. Environ.* **2022**, *288*, 119297. [CrossRef]

35. Abbaszadeh, M.; Soltani-Mohammadi, S.; Ahmed, A.N. Optimization of Support Vector Machine Parameters in Modeling of Iju Deposit Mineralization and Alteration Zones Using Particle Swarm Optimization Algorithm and Grid Search Method. *Comput. Geosci.* **2022**, *165*, 105140. [CrossRef]

36. Guo, B.; Zhang, D.; Pei, L.; Su, Y.; Wang, X.; Bian, Y.; Zhang, D.; Yao, W.; Zhou, Z.; Guo, L. Estimating $PM_{2.5}$ Concentrations via Random Forest Method Using Satellite, Auxiliary, and Ground-Level Station Dataset at Multiple Temporal Scales across China in 2017. *Sci. Total Environ.* **2021**, *778*, 146288. [CrossRef]

37. Bera, B.; Bhattacharjee, S.; Sengupta, N.; Saha, S. $PM_{2.5}$ Concentration Prediction during COVID-19 Lockdown over Kolkata Metropolitan City, India Using MLR and ANN Models. *Environ. Challenges* **2021**, *4*, 100155. [CrossRef]

38. She, L.; Zhang, H.K.; Li, Z.; de Leeuw, G.; Huang, B. Himawari-8 Aerosol Optical Depth (Aod) Retrieval Using a Deep Neural Network Trained Using Aeronet Observations. *Remote Sens.* **2020**, *12*, 4125. [CrossRef]

39. Zhao, X.; Shi, H.; Yang, P.; Zhang, L.; Fang, X.; Liang, K. Inversion Algorithm of $PM_{2.5}$ Air Quality Based on Nighttime Light Data from NPP-VIIRS. *J. Remote Sens.* **2017**, *21*, 291–299. [CrossRef]

40. Li, K.; Liu, C.; Jiao, P. Estimating of Nighttime $PM_{2.5}$ Concentrations in Shanghai Based on NPP/VIIRS Day_Night Band Data. *Acta Sci. Circumstantiae* **2019**, *39*, 1913–1922. [CrossRef]

41. Chen, H.; Xu, Y.; Mo, Y.; Zhang, Y.; Yang, Z. Estimating Nighttime $PM_{2.5}$ Concentrations in Huai'an Based on NPP/VIIRS Nighttime Light Data. *Acta Sci. Circumstantiae* **2022**, *42*, 342–351. [CrossRef]

42. Sager, L. Estimating the Effect of Air Pollution on Road Safety Using Atmospheric Temperature Inversions. *J. Environ. Econ. Manag.* **2019**, *98*, 102250. [CrossRef]

43. Wei, J.; Li, Z. *ChinaHighPM2.5: Big Data Seamless 1 km Ground-Level PM2.5 Dataset for China*; Version 4; Data Set; Zenodo: Geneva, Switzerland, 2019. [CrossRef]

44. Wei, J.; Li, Z.; Cribb, M.; Huang, W.; Xue, W.; Sun, L.; Guo, J.; Peng, Y.; Li, J.; Lyapustin, A.; et al. Improved 1 Km Resolution $PM_{2.5}$ Estimates across China Using Enhanced Space-Time Extremely Randomized Trees. *Atmos. Chem. Phys.* **2020**, *20*, 3273–3289. [CrossRef]

45. Kieffer, H.H.; Anderson, J.M. Use of the Moon for Spacecraft Calibration over 350 to 2500 Nm. In *Sensors, Systems and Next-Generation Satellites II*; SPIE: Bellingham, WA, USA, 1998; Volume 3498, pp. 325–336. [CrossRef]

46. Kieffer, H.H.; Stone, T.C. The Spectral Irradiance of the Moon. *Astron. J.* **2005**, *129*, 2887–2901. [CrossRef]